L-Band Pulse Phase Measurements of Pulsar B0329+54 Using a 1.8 m Dish Antenna

Ryan McKnight, *Graduate Student Member, IEEE*, Brian C. Peters, *Graduate Student Member, IEEE*, Sabrina Ugazio, *Member, IEEE*, and Frank van Graas, *Senior Member, IEEE*

***Abstract*—Pulsars are rotating neutron stars that emit stable periodic signals. In this work, pulsar pulse phase measurements were performed using a dish antenna with a diameter of 1.8 m with the goal to characterize the repeatability of pulsar timing measurements using a small-aperture antenna. A low-cost data collection system using a software-defined radio was designed and implemented in support of this goal. The instrumentation was used to observe pulsar B0329+54 for a time span of just over 19 hours at an observation frequency of 1400 MHz. Nine independent phase measurements were performed with an integration time of 1 h each. A probabilistic method using an M-of-N search algorithm was used to conclude that the pulsar was successfully detected with a false detection probability of less than 1.4×10^{-4} and that 7 out of the 9 phase measurements were successful. The standard deviation of the successful measurements was 1.4 ms.**

***Index Terms*—Pulsar, timing, radio astronomy.**

I. Introduction

PULSARS were first discovered in 1967 by Hewish, Bell, et al. at the Mullard Radio Astronomy Observatory near Cambridge, U.K. [1]. A pulsar is a rotating neutron star emitting a high-energy beam of electromagnetic radiation which is not necessarily aligned with its rotation axis. As the pulsar rotates, the beam sweeps through space and is observed at a distance as a series of short, regular pulses [2]. To date, over 3800 individual pulsars have been identified [3], each with a unique pulse period and signal profile determined by the characteristics of the neutron star. Typically, the pulse periods range from just a few milliseconds to several seconds. Most known pulsars emit in the radio region of the electromagnetic spectrum, with a smaller subset visible at optical, X-ray, and gamma wavelengths [2].

Due to the large rotational mass of a pulsar, their pulse frequencies are stable. Although terrestrial frequency standards are a few orders of magnitude more stable in timing, pulsars could provide an independent check on long-term terrestrial timescale variations [4], have proven useful for gravitational wave studies [5], and are being studied for interstellar space navigation [6]. Pulsars are often observed on Earth by large radio telescopes such as the $100\,\mathrm{m}$ Green Bank Telescope (GBT) at the Green Bank Observatory in West Virginia. These observatories perform searches to discover and catalog new pulsars and produce timing models that can be used to predict the pulse phase and frequency of a known pulsar signal at a given time. Position, velocity, and time (PVT) estimation using pulsars involves performing a measurement of the pulse phase and/or frequency and computing its deviation from a prediction produced by a timing model. This process generally requires a coarse initial estimate of the user's PVT, which can be refined over time using a statistical estimation process such as a Kalman filter [7], [8].

NASA's Station Explorer for X-ray Timing and Navigation Technology (SEXTANT) experiment aboard the International Space Station (ISS) has successfully demonstrated pulsar phase and frequency measurements in space from low-Earth orbit (LEO), using X-ray measurements from 4 pulsars to achieve autonomous, real-time navigation with $< 10\,\mathrm{km}$ root-sum-squared (RSS) navigation error [9]. Additionally, simulations show that similar performance could be achieved in geostationary orbit (GEO) or in a lunar near rectilinear halo orbit (NRHO) [10]. Pulsar timing could also be performed at the radio-frequency (RF) bands, as first suggested by [11], with the advantage that specialized X-ray hardware is not needed to perform phase and frequency measurements. For terrestrial users, RF signals are the only suitable option for pulsar measurements since X-ray pulsar signals are not able to penetrate the Earth's atmosphere.

The primary challenge for pulsar timing is the weak signal strength. While large telescopes such as the GBT can directly measure the pulsar signal, small-aperture antennas require the use of long integration techniques to raise the signal-to-noise ratio (SNR) to a level sufficient to perform the measurements. When using a small-aperture (less than $20\,\mathrm{m}^2$) antenna, the signal is well below the noise floor due to the large distance (on the order of thousands of light-years) from the Earth to known pulsars [12]. The accuracy of a pulsar timing measurement is a function of both the antenna aperture and the integration time used to perform the measurement, among other parameters (more detail is provided in Section VI). A review of the existing literature on RF pulsar navigation and timing was previously carried out by the authors in [13]. Publications such as [12], [14] suggest that timing measurements with an accuracy on the order of 10 to $100\,\mu\mathrm{s}$ may be feasible using an antenna with an effective aperture on the order of $10\,\mathrm{m}^2$ and an integration time on the order of a few hours. The ability to accurately measure pulse phase using such a small antenna would enable a broad range of timing applications for terrestrial users. Additionally, such an antenna is near the size that is commonly used for RF

Ryan McKnight, Brian C. Peters, and Sabrina Ugazio are with the School of Electrical Engineering and Computer Science, Ohio University, Athens, OH 45701 USA.

Frank van Graas is with the Department of Electrical and Computer Engineering, Air Force Institute of Technology, WPAFB, OH 45433 USA.

communications on-board spacecraft. At this scale, spacecraft could utilize the same set of hardware for RF communications and pulsar measurements, eliminating the need for dedicated X-ray detector equipment.

In a previous publication by the authors [15], an experiment was outlined to observe pulsars using a dish antenna with an effective aperture of less than $10\,\mathrm{m}^2$ and analyze the measurement accuracy that could be obtained with such a system. In that work, a high-level design for the experiment was included, and a performance analysis was performed. In a follow-up study [16], simulated pulsar data were used to develop and test the phase measurement techniques for the experiment.

The present work makes the following two contributions.

1) Design, implement, and evaluate instrumentation to receive an RF pulsar at L-band using a small ($1.45\,\mathrm{m}^2$ effective aperture) antenna.
2) Perform pulse phase measurements and characterize their repeatability.

The article is structured as follows: Section II provides a high-level overview of the experiment. Section III outlines the theoretical background of pulsar timing. Section IV provides the theoretical background for the phase measurement process. Section V describes the setup of the experiment and the software used to collect the data. Section VI details the analysis of the collected data and presents the results. Finally, Section VII summarizes the findings and provides recommendations for future study.

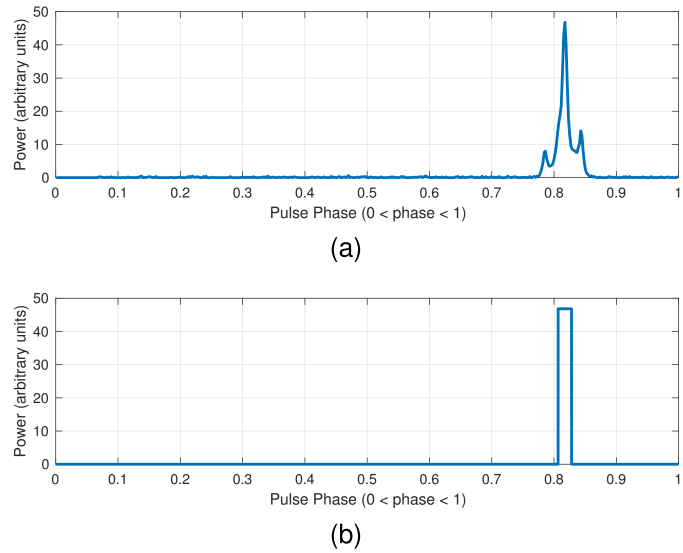

Fig. 1. (a) template pulse profile for B0329+54 as recorded at $1410\,\mathrm{MHz}$ by the Effelsberg $100\,\mathrm{m}$ radio telescope [19]. Profile downloaded from the EPN Pulse Profile Database [20] in EPN format [21]. (b) idealized "top-hat" version of the pulse profile with the same time-average and maximum value as the template profile (see Section IV). The ratio P/W is equal to 46.7. Both profiles are normalized to have unit mean.

II. Experiment Overview

An experiment was conducted on 8 June 2024 near McArthur, OH at a site chosen to reduce the potential impact of radio-frequency interference (RFI). Pulsar B0329+54 was observed for $19.22\,\mathrm{h}$, resulting in approximately $9.05\,\mathrm{h}$ of useful data for phase measurements. B0329+54 was selected for observation because it has the strongest signal of any pulsar visible in the northern hemisphere at $1400\,\mathrm{MHz}$. The observation center frequency was chosen as $1400\,\mathrm{MHz}$ because of the ability to repurpose an existing L-band data collection setup and the common use of $1400\,\mathrm{MHz}$ for radio astronomical observations. The International Telecommunication Union (ITU) designates 1370 to $1427\,\mathrm{MHz}$ as a preferred frequency band for radio astronomical measurements due to its proximity to the Hydrogen line frequency [17]. Pulsar B0329+54 has a nominal pulse period of approximately $0.715\,\mathrm{s}$. Additionally, its pulse profile has a relatively sharp peak, with a pulse width (defined as the width at 50% of its peak power) of $6.6\,\mathrm{ms}$ [18], which is beneficial for measurement purposes. Further details of the pulsar selection are given in [15].

The experiment used a software-defined radio (SDR) to record RF in-phase/quadrature (I/Q) samples. The use of an SDR allows for signal samples to be recorded over a period of several hours and stored to disk for later processing and analysis. A National Instruments Universal Software Radio Peripheral (USRP) X310 with a TwinRX daughterboard was chosen due to its high sampling rate ($100\,\mathrm{Msps}$) and integrated GPS-disciplined oscillator (GPSDO). This design choice provides a favorable observation bandwidth of 1350 to $1450\,\mathrm{MHz}$ at the $1400\,\mathrm{MHz}$ center frequency. The GPSDO enables each of the samples to be tagged with a Coordinated Universal Time (UTC) time stamp, allowing for the relative accuracy of pulsar phase measurements to be characterized over long time spans.

III. Pulsar Timing

Pulsars emit periodic signals, each one with a unique spin frequency and power profile shape. While the power profile for a given pulsar can vary from one period of the signal to another, the average power profile across a few hundred to a few thousand pulse periods is remarkably stable [2]. Pulsar B0329+54 has a nominal period of $0.715\,\mathrm{s}$ and a power profile that is displayed in Fig. 1a. A simple pulsar timing model can be described by three parameters at a given epoch: a nominal pulse frequency and its first and second time derivatives, denoted as f_0, f_1, and f_2. By convention, these parameters are referenced to the solar system barycenter (SSB). The timing model is formed by measuring pulse time of arrivals (TOAs) over a period of time and fitting the parameters to the measurements. The TOA measurements are made by performing a phase offset measurement between the observed pulsar signal and a known template pulse, such as that shown in Fig. 1a. For power calculation purposes, the pulsar profile can be approximated by a top-hat shape with a period of P and a width of W, as shown in Fig. 1b. The set of timing parameters used for this work were generated by the $76\,\mathrm{m}$ Lovell Radio Telescope at the Jodrell Bank Observatory [22] and obtained from the Australia Telescope National Facility (ATNF) Pulsar Catalogue [3]. Parameters for B0329+54 are listed in Table I.

The timing model parameters can be propagated forward to predict the phase and frequency of the pulsar signal at a given time. These predictions can be referenced to the location of the observer instead of the SSB by regarding the

TABLE I
KEY PARAMETERS FOR PULSAR B0329+54 FROM [18], [22], [23].

Param	Description	Value	Uncertainty
f_0	Pulse freq. at epoch	$1.3995\,\text{Hz}$	6×10^{-12}
f_1	1st deriv. of pulse freq.	$-4.0\times10^{-15}\,\text{Hz/s}$	14×10^{-21}
f_2	2nd deriv. of pulse freq.	$5.3\times10^{-28}\,\text{Hz/s}^2$	15×10^{-29}
Epoch	Epoch for f_0, f_1, f_2	12 February 1986	–
DM	Dispersion measure	$26.7641\,\text{cm}^{-3}\cdot\text{pc}$	1×10^{-4}
W_{50}	Pulse width (50% of peak)	$6.6\,\text{ms}$	–
S_{1400}	Flux density (1400 MHz)	$203\,\text{mJy}$	57

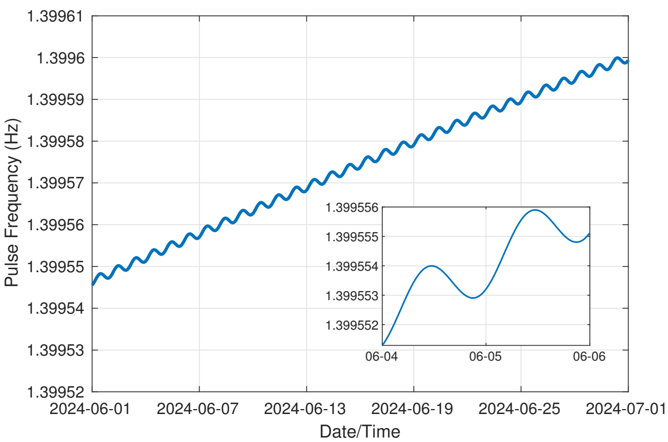

Fig. 2. Pulse frequency for B0329+54 at the observing site during the month of June 2024 computed using the timing model parameters in Table I. A portion of the long-term oscillation appears as a steady increase during the month. The short-term oscillation can be seen more clearly in the detail view inset.

pulsar signal as a uniform plane wavefront, which is a valid approximation due to the large distance between the Earth and the pulsar. The predicted pulse phase and frequency at the location of the observer, which vary as a function of time, will be denoted as $\phi(t)$ and $f(t)$. $f(t)$ varies with time not only because of its non-zero time derivatives, but also due to the Doppler effect. Fig. 2 displays a plot of $f(t)$ vs. time for B0329+54 in McArthur, OH during the month of June 2024. The Doppler effect causes a long-term sinusoidal oscillation with a period of 1 year due to the Earth's orbit around the Sun. During June 2024 at this particular location, the long-term oscillation manifested as an average drift of approximately $1.7\times10^{-6}\,\text{Hz/d}$. An additional oscillation with a period of $24\,\text{h}$ results from Earth's rotation about its axis. It rides on top of the long-term oscillation and has a peak-to-peak magnitude of approximately $2\times10^{-6}\,\text{Hz}$. The units of $f(t)$ are Hz. By convention, $\phi(t)$ is defined as the time-integral of $f(t)$: as such, it is a dimensionless quantity with units of cycles such that one cycle corresponds to one pulse period. Because $f(t)$ is not constant, $\phi(t)$ does not advance at a constant rate with respect to time. In other words, the length of each pulse period (measured in seconds) varies with time. The timing model parameters and the location of the observer can be provided to the open-source pulsar timing software TEMPO2 [24] to generate a convenient set of polynomial coefficients that can be used to approximate $\phi(t)$ and $f(t)$ at a given time.

The definition of $\phi(t)$ necessarily depends on the choice of a specific fiducial point on the template pulse used to form the TOA measurements. This point corresponds to $\phi(t)=0$. In the present work, an arbitrary fiducial point is used because the objective is to compare relative phase differences between successive measurements to characterize their repeatability.

Pulsar signals are affected by frequency dispersion as they propagate through the ionized component of the interstellar medium (ISM) such that upper band frequencies of the signal at $1450\,\text{MHz}$ arrive at the observer prior to the lower band frequencies at $1350\,\text{MHz}$. The amount of dispersion is approximately proportional to the distance from the observer to the pulsar [2]. It is commonly characterized by a value known as the dispersion measure (DM), which is unique to a particular pulsar and has units of $\text{cm}^{-3}\cdot\text{pc}$ where pc denotes a parsec, a unit of distance approximately equal to 3.26 light-years. The DM for B0329+54 is given by [23] and obtained from the ATNF catalogue (see Table I). Using this value, the relative time shift between the pulse arrival time observed at two separate frequencies f_1 and f_2 can be calculated using the following equation [2]:

$$\Delta t = \mathcal{D}\times\left(f_1^{-2}-f_2^{-2}\right)\times\text{DM} \tag{1}$$

where $\mathcal{D}$ is defined as $1/(2.41\times10^{-16}\,\text{Hz}^{-2}\cdot\text{pc}\cdot\text{cm}^{-3}\cdot\text{s}^{-1})$.

For the experiment conducted in this work, the observation bandwidth is $100\,\text{MHz}$. The maximum relative time shift within the observing band can be obtained by setting f_1 and f_2 to the band edges: $1350\,\text{MHz}$ and $1450\,\text{MHz}$, resulting in $\Delta t = 8.11\,\text{ms}$. Since the width of the pulse at 50% of its maximum power is only $6.6\,\text{ms}$ (see Table I), it is necessary to correct the pulse dispersion to prevent the signal power from being smeared in time, reducing the overall SNR. This correction is implemented by a process known as incoherent dedispersion, which involves dividing the pulsar signal samples into a number n_{chan} of frequency channels using the discrete Fourier transform (DFT) and applying a corrective time shift to each channel [2], [25]. The process of splitting the data into multiple frequency channels using the DFT is known as a software filterbank.

Because of the low pulsar signal strength received by a small-aperture antenna, non-coherent long integration of the signal over a time span t_{int} must be performed in order to detect and measure it. This process is referred to as folding [2] and is depicted in Fig. 3. It takes advantage of the periodic nature of the pulsar signal: it is assumed that the signal has a power profile that can be described by a continuous function $s(\phi(t))$ where s is a periodic function of phase such that $s(\phi(t)) = s(\phi(t)+n)$ for all integers n. The process involves assigning each time sample of the recorded data to one of n_{bins} individual bins, numbered 0 to $n_{\text{bins}}-1$. Each bin represents the average emission of the pulsar at a particular pulse phase between 0 and 1, referred to as the phase-center of the bin. The phase-center ϕ_n of bin n is given by the following expression:

$$\phi_n = (n+0.5)/n_{\text{bins}} \tag{2}$$

The bin number assigned to a sample, given its sample time t, is $\lfloor(\phi(t) \bmod 1)\,n_{\text{bins}}\rfloor$, where $\lfloor\cdot\rfloor$ denotes the floor function.

After each sample has been assigned a bin number, the complex power (given by I^2+Q^2) of all the samples that

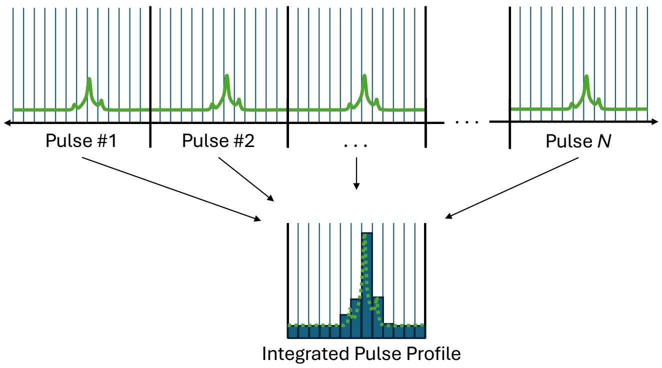

Fig. 3. An illustration of the folding process. The vertical lines mark the boundaries between individual bins. All samples within each bin are averaged to form the integrated pulse profile.

fall within each of the individual bins are averaged to form an integrated pulse profile. The integrated pulse profile contains n_{bins} samples with units of power and represents the average emission of the pulsar as a function of its pulse phase. The result of this process is an SNR improvement that scales as a factor of $\sqrt{t_{\text{int}}/n_{\text{bins}}}$ (see Section VI for details).

The folding process is performed separately for each of the n_{chan} frequency channels present in the data, resulting in n_{chan} unique integrated pulse profiles, each containing n_{bins} samples. The integrated pulse profile values for channel i are denoted as $p_i[n]$, where i ranges from 0 to $n_{\text{chan}} - 1$ and n ranges from 0 to $n_{\text{bins}} - 1$. The DFT of $p_i[n]$ is denoted as $P_i[k]$, where k ranges from $-n_{\text{bins}}/2 + 1$ to $n_{\text{bins}}/2$. In order to form a single unified integrated pulse profile, denoted as $p[n]$ with DFT $P[k]$, the dispersion delay in each channel must be corrected. First, the dispersion delay Δt_i for each channel i (with channel frequency f_i) relative to the observation center frequency f_c is calculated using (1) by setting $f_1 = f_c$ and $f_2 = f_i$. Since each integrated pulse profile represents samples of a periodic signal, a circular time shift of $-\Delta t_i$ is applied to each one in order to correct for the dispersion delay. The circular time shift can be applied in the frequency domain by using the DFT shift theorem [26], in which a circular shift in the time domain is represented by adding a linear ramp to the phase of the discrete Fourier coefficients:

$$P[k] = \sum_{i=0}^{n_{\text{chan}}-1} P_i[k] e^{-j2\pi \Delta t_i k / T_0} \tag{3}$$

where T_0 is the average pulse period during the data collection. $p[n]$ can be computed from $P[k]$ via the inverse DFT.

After the dedispersion and folding process is complete, a pulse phase measurement is performed by estimating the relative phase shift between the integrated pulse profile (generated by the folding process) and a known template profile such as the one displayed in Fig. 1a. If the timing model used to generate $\phi(t)$ for the folding process is accurate, the phase shift is primarily a function of the observer's clock bias. The phase measurement can be used as part of a process to estimate this clock bias, effectively synchronizing the observer's local clock to a known source. Fig. 4 summarizes the steps in the process of estimating a clock bias using RF pulsar observations.

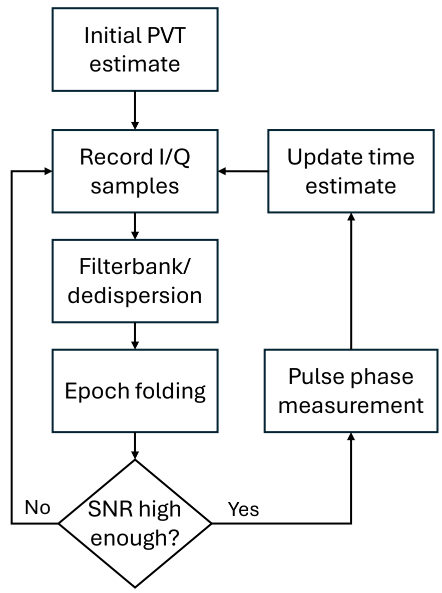

Fig. 4. Iterative process of recording samples of a pulsar signal, forming an integrated pulse profile, measuring the pulse phase, and updating the user's time estimate.

Propagation of the timing model parameter uncertainties listed in Table I from the epoch date to the date of the experiment indicate that $f(t)$ can be accurately predicted to within 1.3×10^{-10} Hz, which is sufficient to perform the folding process. While the uncertainty on the prediction of $\phi(t)$ is 0.06, a significant portion of a full pulse period, this is inconsequential because it is already assumed that the reference point $\phi(t) = 0$ is arbitrary. As mentioned earlier in this section, only relative phase measurements are considered in this work.

IV. Measuring Pulse Phase

As discussed in Section III, the output of the folding process is an integrated pulse profile for each of the n_{chan} frequency channels, each represented by a sequence of n_{bins} real, discrete-time samples with units of power. A single frequency channel is considered first for simplicity.

Three discrete-time signals, $p[n]$, $s[n]$, and $g[n]$, are defined, where n ranges from 0 to $n_{\text{bins}} - 1$:

$$p[n] = a + bs[n] + g[n] \tag{4}$$

$p[n]$ represents the integrated pulse profile samples for each bin. $s[n]$ represents samples of the template pulse profile. It is formed by sampling the continuous-phase function $s(\phi)$ at the bin phase-centers given by (2). $s(\phi)$ can be approximated by phase-interpolating samples of the template signal displayed in Fig. 1a. In (4), a and b represent a constant DC offset and scaling factor, respectively, and $g[n]$ represents the power ($I^2 + Q^2$) of a complex Gaussian noise signal with the DC offset removed (absorbed into a). Note that $p[n]$, $s[n]$ and $g[n]$ are each real-valued signals with units of power.

The complex-valued DFTs of signals $p[n]$, $s[n]$, and $g[n]$ are denoted by $P[k] = P_k e^{j\theta_k}$, $S[k] = S_k e^{j\phi_k}$, and $G[k] = G_k e^{j\psi_k}$, respectively, where k ranges from $-n_{\text{bins}}/2 + 1$ to

$n_{\text{bins}}/2$. Equation (4) can be represented in the frequency domain:

$$P_k e^{j\theta_k} = a n_{\text{bins}} + b S_k e^{j\phi_k} + G_k e^{j\psi_k} \tag{5}$$

Equations (4) and (5) assume that the phase prediction $\phi(t)$ used to perform the folding process is error-free. In practice, it should be assumed that the local clock offset produces an offset in $\phi(t)$, denoted by ϕ_{off}. It is assumed that the local clock has sufficient stability that ϕ_{off} can be considered constant during the folding period. The result of the offset is a relative phase shift between the integrated pulse profile and the template pulse profile. Following [27], (5) is modified to include this offset:

$$P_k e^{j\theta_k} = a n_{\text{bins}} + b S_k e^{j\phi_k + j2\pi k \phi_{\text{off}}} + G_k e^{j\psi_k} \tag{6}$$

The modification utilizes the DFT shift theorem described in Section III. Still following [27], the phase offset estimate $\hat{\phi}_{\text{off}}$ can be determined by the following minimization:

$$\hat{\phi}_{\text{off}} = \arg\min_{\phi_{\text{off}}} \sum_{k=1}^{n_{\text{bins}}/2} -P_k S_k \cos(\phi_k - \theta_k + k2\pi\phi_{\text{off}}) \tag{7}$$

This frequency-domain estimation process is conceptually similar to performing a time-domain circular cross-correlation between $p[n]$ and $s[n]$, but allows for better time resolution [28]. It is straightforward to solve (7) by using Brent's method [29] or other standard minimization techniques.

Now considering all n_{chan} frequency channels, dedispersion (as described in Section III) must be performed before the phase offset estimation. The dispersion-corrected integrated pulse profile DFT coefficients $P[k]$ given by (3) are used directly in (6) and (7). The rest of the estimation process is unmodified.

Following [30], the SNR of $p[n]$ is defined by assuming that the pulsar signal has an ideal top-hat shape with the same peak and time-average power as the real signal (see Fig. 1b). The SNR is then equal to the ratio of the on-pulse power of the top-hat signal to the standard deviation of the noise power $g[n]$. By this definition, a pulsar with a given time-average flux density will have a higher SNR if its power profile has a sharper peak. The sharpness can be characterized by the ratio of the length of the period to the width of the top hat pulse, denoted as P/W. A higher P/W ratio will result in a higher SNR. Since a real pulsar profile does not have an ideal top-hat shape, P/W is approximated by dividing the maximum value of the real profile by its average value during one period. For the profile in Fig. 1a, P/W is approximated as 46.7. To estimate the SNR, it is necessary to find estimates of the constants a and b in (4). The phase offset estimate $\hat{\phi}_{\text{off}}$ can be used to directly calculate the parameter estimates $\hat{a}$ and $\hat{b}$ using the following equations [27]:

$$\hat{b} = \sum_{k=1}^{n_{\text{bins}}/2} P_k S_k \cos\left(\phi_k - \theta_k + k2\pi\hat{\phi}_{\text{off}}\right) / \sum_{k=1}^{n_{\text{bins}}/2} S_k^2 \tag{8}$$

$$\hat{a} = \left(P_0 - \hat{b} S_0\right) / n_{\text{bins}} \tag{9}$$

Following (4), the noise samples $g[n]$ can be estimated by subtracting the estimated DC offset $\hat{a}$ and $\tilde{s}[n]$, which represents a phase-shifted template signal formed by sampling the continuous-phase function $\tilde{s}(\phi) = s(\phi + \hat{\phi}_{\text{off}})$ at the bin phase-centers given by (2), from $p[n]$. The estimated noise samples are denoted $\hat{g}[n]$:

$$\hat{g}[n] = p[n] - \hat{a} - \hat{b}\tilde{s}[n] \tag{10}$$

Assuming that $s(\phi)$ has been normalized to have unit mean, the SNR estimate is given by the following equation:

$$\hat{\text{SNR}} = (P/W)\hat{b}/\sigma_{\hat{g}} \tag{11}$$

where $\sigma_{\hat{g}}$ is the standard deviation of the samples of $\hat{g}$.

V. Data Collection

The antenna used for the data collection was a solid dish with a diameter of $1.8\,\mathrm{m}$ mounted to a pedestal on a trailer for portable operation, equipped with a dual-linear polarization L-band horn feed and a WanTcom WBA1216ASBT low-noise amplifier (LNA). Only one polarization was used for the experiment. The dish, feed, and mount were repurposed from a setup previously used for global navigation satellite systems (GNSS) signal characterization and monitoring. The antenna gain was measured to be $G_a = 27\,\mathrm{dBi}$ at GPS L1 frequency ($1575.42\,\mathrm{MHz}$) [31], which is equivalent to an effective aperture of $1.45\,\mathrm{m}^2$ using the relation $G_a = 4\pi A_e/\lambda^2$. The half-power beamwidth of the antenna is $7.2°$. Two motors and a programmable rotator controller provide azimuth and elevation pointing with an elevation range of approximately $25°$ to $77°$ and a total azimuth range of $300°$. The data were recorded using a USRP X310 SDR at a sample rate of $100\,\mathrm{Msps}$ (I/Q). A 48-thread HP ProLiant server with $96\,\mathrm{GB}$ of RAM was used to control the SDR and rotator controller. The data were stored on a QNAP network-attached storage (NAS) system connected to the server using a network interface. The USRP, server, NAS, and rotator controller were rack-mounted and housed inside a vehicle for protection from the outdoor elements. AC power was provided to the equipment via an extension cable from a nearby cabin. A photo of the setup is shown in Fig. 5, and a block diagram of the instrumentation is provided in Fig. 6.

Before starting the experiment, site surveys were conducted by sweeping the dish around its azimuth and elevation travel while using the SDR to monitor the spectrum within the band of interest (1350 to $1450\,\mathrm{MHz}$), revealing a clean, flat noise floor.

The L-band setup comes with the advantage of pointing calibration using GNSS satellites. A coarse calibration of the azimuth and elevation angles was performed by carefully leveling the platform and using a magnetic compass. A fine calibration was then performed by connecting a commercial GNSS receiver to the antenna and performing azimuth and elevation sweeps across GPS or Wide Area Augmentation System (WAAS) satellites with known positions. The carrier-to-noise density ratio (CN0) was logged as a function of the pointing angles and used to fine-tune the calibration. After the calibration was complete, it was estimated by further sweeps of GNSS satellites that the pointing accuracy was better than $1°$, which is well within the $7.2°$ half-power beamwidth of the antenna.

Fig. 5. The data collection equipment setup at the observation site. The dish has a diameter of $1.8\,\mathrm{m}$. It is mounted on a trailer and has an effective aperture of approximately $1.45\,\mathrm{m}^2$. The SDR, server, and NAS are mounted to an equipment rack inside the vehicle.

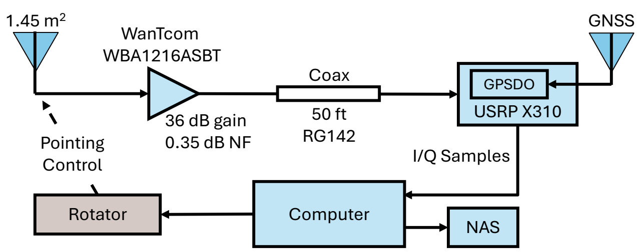

Fig. 6. Block diagram of the RF hardware system.

The SDR streamed time-tagged I/Q samples using 16 bits each for I and Q to the server at a rate of $100\,\mathrm{Msps} \times 32\,\mathrm{bits/sample} = 3.2\,\mathrm{Gbps}$. The use of a 10 gigabit network interface controller (NIC) on the server was required to support this sample rate. It was decided not to store the raw I/Q samples to disk due to the high data rate (equivalent to $1.44\,\mathrm{TB/h}$). Instead, the data were pre-integrated by a factor of 100 in real-time to reduce the rate. It is necessary to perform the pre-integration separately for each frequency channel, requiring the software filterbank described in Section III to run in real-time. The filterbank employs a fast Fourier transform (FFT) of length 500 utilizing a Bartlett window and an overlap of half the FFT length [25], [29]. The data were recorded, processed, and stored by a custom-developed software program that used a parallel processing architecture, taking advantage of the server's 48 CPU threads. The use of this parallel architecture was necessitated by the high rate of data ingested from the SDR. After the filterbank and pre-integration, the complex power ($I^2 + Q^2$) of each FFT point was stored to disk as a 32-bit floating point number. A block diagram depicting the real-time data processing software is displayed in Fig. 7. Data were stored to disk at a rate of $100\,\mathrm{Msps} \times 2/100 \times 4\,\mathrm{bytes/sample} = 8\,\mathrm{MB/s}$ where the factor of 2 is due to the FFT overlapping, or about $28.8\,\mathrm{GB/h}$.

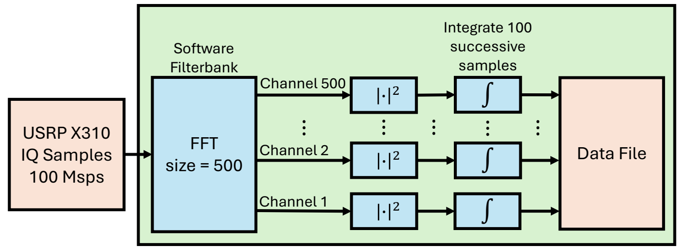

Fig. 7. Block diagram of the data collection setup. A 48-thread server is used to perform the software filterbank and integration process in real-time to reduce the amount of data stored to disk by a factor of 50.

In the field of radio astronomy, it is common to characterize the spectral flux density of celestial sources in units of Janskys (Jy), where $1\,\mathrm{Jy} = 10^{-26}\,\mathrm{W \cdot m^{-2} \cdot Hz^{-1}}$. It is also common to characterize the gain of the receiver in units of $\mathrm{K/Jy}$, computed as:

$$G = A_\mathrm{e}/(2k_\mathrm{B}) \tag{12}$$

where A_e is the effective aperture of the antenna in m^2 and k_B is the Boltzmann constant ($1381\,\mathrm{Jy \cdot m^2/K}$). For the receiver used in this experiment, $G = 5.24 \times 10^{-4}\,\mathrm{K/Jy}$. The total noise temperature T_sys of the observation system can be estimated by the following equation [2]:

$$T_\mathrm{sys} = T_\mathrm{rec} + T_\mathrm{spill} + T_\mathrm{atm} + T_\mathrm{sky} \tag{13}$$

T_spill is assumed to be $10\,\mathrm{K}$, and T_atm is assumed to be negligible [2]. T_sky is a function of the observation frequency and the pulsar's position on the celestial sphere, and can be computed using datasets such as that given by [32]. For B0329+54 at $1400\,\mathrm{MHz}$, $T_\mathrm{sky} = 4.3\,\mathrm{K}$. The receiver noise temperature can be computed using the Friis formula for noise temperature [33]:

$$T_\mathrm{rec} = T_1 + \frac{T_2}{G_1} + \frac{T_3}{G_1 G_2} + \cdots \tag{14}$$

where G_i and T_i are the gain and noise temperature, respectively, of component i. Using the values in Table II, T_rec is computed to be $33.1\,\mathrm{K}$, and T_sys is computed to be $47.4\,\mathrm{K}$.

TABLE II
GAIN AND NOISE FIGURE FOR RECEIVER COMPONENTS.

Component	Line Loss Before LNA	LNA	RG142 Coax	USRP X310 with TwinRX
Gain	$-0.10\,\mathrm{dB}$	$36.00\,\mathrm{dB}$	$-8.00\,\mathrm{dB}$	$0.00\,\mathrm{dB}$
Noise Figure	$0.10\,\mathrm{dB}$	$0.35\,\mathrm{dB}$	$8.00\,\mathrm{dB}$	$5.00\,\mathrm{dB}$

Key parameters of the data collection are summarized in Table III.

VI. RESULTS AND ANALYSIS

As mentioned in Section II, the data collection was started on 8 June 2024 and ran for a total of $19.22\,\mathrm{h}$, producing a data file with a total size of $553\,\mathrm{GB}$. The azimuth and elevation angles used to track the pulsar during the data collection are displayed in Fig. 8. As shown in Fig. 8a, the pulsar appears in the Northern portion of the sky because its declination angle

TABLE III
KEY PARAMETERS FOR THE DATA COLLECTION.

Location	McArthur, OH
Observation Center Frequency	$1400\,\mathrm{MHz}$
Sample Rate (I/Q)	$100\,\mathrm{Msps}$
Effective Antenna Aperture	$1.45\,\mathrm{m}^2$
Antenna Gain	$5.24 \times 10^{-4}\,\mathrm{K/Jy}$
Estimated System Noise Temperature	$47.4\,\mathrm{K}$
Polarization	linear
Number of Filterbank Channels	500

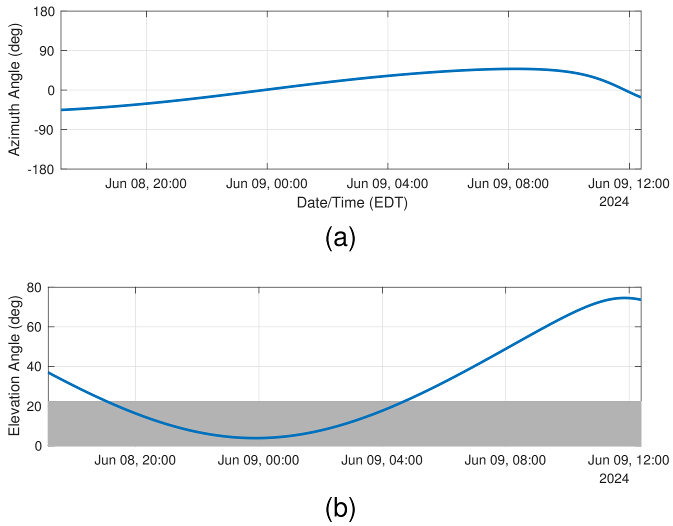

Fig. 8. (a) Azimuth and (b) Elevation angles for pulsar B0329+54 at the observation site during the data collection. Azimuth angle is measured from North towards East. The total time span is $19.22\,\mathrm{h}$. The shaded region of the elevation plot represents the elevation mask of $22.5°$. The pulsar was below the mask for $9.67\,\mathrm{h}$, and above the mask for $9.55\,\mathrm{h}$.

(around $55°$) is greater than the latitude of the observation (around $39°$). As shown in Fig. 8b, the pulsar never sets below the horizon at this location, reaching a minimum elevation angle of approximately $3.9°$.

Before analyzing the data, it is necessary to mask certain portions which are detrimental to the observation and measurement of the pulsar. When a data point is masked, it is replaced with zero. Frequency channels within approximately $5\,\mathrm{MHz}$ of the upper and lower band edges were masked due to a notable roll-off in the frequency response of the RF front end of the SDR. An elevation mask of $22.5°$ was applied to the data due to the $25°$ minimum elevation travel angle of the rotator and the $7.2°$ half-power beamwidth of the antenna. Despite the relatively clean RF environment at the chosen observation site, minor portions of the data contain some apparent effects of RFI. Approximately 15 minutes at the beginning and end of the data collection were masked due to the presence of cellular phones in the vicinity of the experiment during set-up and tear-down, which contributed to RFI levels. For the remainder of the data, an RFI detection and masking algorithm was implemented based on the identification of outlier samples in the dataset. The algorithm divided the samples within each frequency channel into time segments equal to the length of one pulse period. Within each segment, the mean, standard deviation, minimum, and maximum values were found, converted to decibels, and plotted as a 2D "waterfall" image. The scale of the statistics is arbitrary, since the power level of the data samples is not calibrated. These images are displayed in Fig. 9. For each of the four statistics, a threshold value was set. If any statistic within a given frequency channel and time segment exceeded its threshold, this portion of the data would be masked. The mask thresholds were hand-adjusted such that portions of the data that appeared to be contaminated by RFI were masked. The complete data mask is displayed in Fig. 10. In total, 58.04% of the data points were masked. The RFI detection algorithm masked 0.73% of the remaining data points after applying the block time, frequency, and elevation masks. Due to the masking, the effective bandwidth of the observation was reduced from $100\,\mathrm{MHz}$ to $89.8\,\mathrm{MHz}$ and the effective integration time was reduced from $19.22\,\mathrm{h}$ to $8.98\,\mathrm{h}$.

The expected post-folding SNR for the observation can be computed using the radiometer equation. The process was described in detail in previous publications by the authors [13], [15], and is summarized here. The radiometer equation for folded observations is given by [30]:

$$\mathrm{SNR} = \frac{SG\sqrt{n_\mathrm{p}\Delta f}}{T_\mathrm{sys}} \frac{\sqrt{t_\mathrm{int}}}{\sqrt{n_\mathrm{bins}}} \frac{P}{W} \tag{15}$$

where S is the pulsar's flux density in units of Jy and G is the receiver gain in units of $\mathrm{K/Jy}$. n_p is the number of independent polarizations averaged (unitless), Δf is the observation bandwidth (Hz) and T_sys is the total system noise temperature (K). This equation makes the assumption that the pulsar signal has an ideal top-hat shape as described in Section IV. The ratio P/W was also defined in Section IV. Using these parameters, which are summarized in Table IV, the expected post-folding SNR is computed to be $9.15\,\mathrm{dB}$ for an integration time of $8.98\,\mathrm{h}$.

TABLE IV
PARAMETERS USED TO COMPUTE EXPECTED SNR.

S	Pulsar flux density at $1400\,\mathrm{MHz}$	$203\,\mathrm{mJy}$
G	Antenna gain	$5.24 \times 10^{-4}\,\mathrm{K/Jy}$
n_p	Number of polarizations	1
Δf	Effective Observation bandwidth	$89.8\,\mathrm{MHz}$
T_sys	Total system noise temperature	$47.4\,\mathrm{K}$
t_int	Effective Integration time	$8.98\,\mathrm{h}$
n_bins	Number of bins used for folding	512
P/W	Period to pulse width ratio	46.7
SNR	**Expected SNR**	$\mathbf{9.15\,dB}$

After the data mask was applied, the folding, dedispersion, and phase offset estimation processes described in Sections III and IV were applied to the data. The resulting integrated pulse profile $p[n]$ is displayed in Fig. 11a. The phase and SNR estimation processes yield results of $\hat{\phi}_\mathrm{off} = 0.38390$ and $\widehat{\mathrm{SNR}} = 5.90$, respectively. Fig. 11b displays $p[n]$ (from Fig. 11a) overlaid with the template profile after phase shifting it by $\hat{\phi}_\mathrm{off}$ (from (7)) and scaling it by $\hat{b}$ (from (8)). The sum term in (7) is plotted as a function of ϕ_off in Fig. 12, demonstrating that $\hat{\phi}_\mathrm{off}$ is the value that minimizes the equation. Although the sharp peak displayed in Fig. 12 is a reasonable indication that a real pulsar signal has been measured, it should be noted

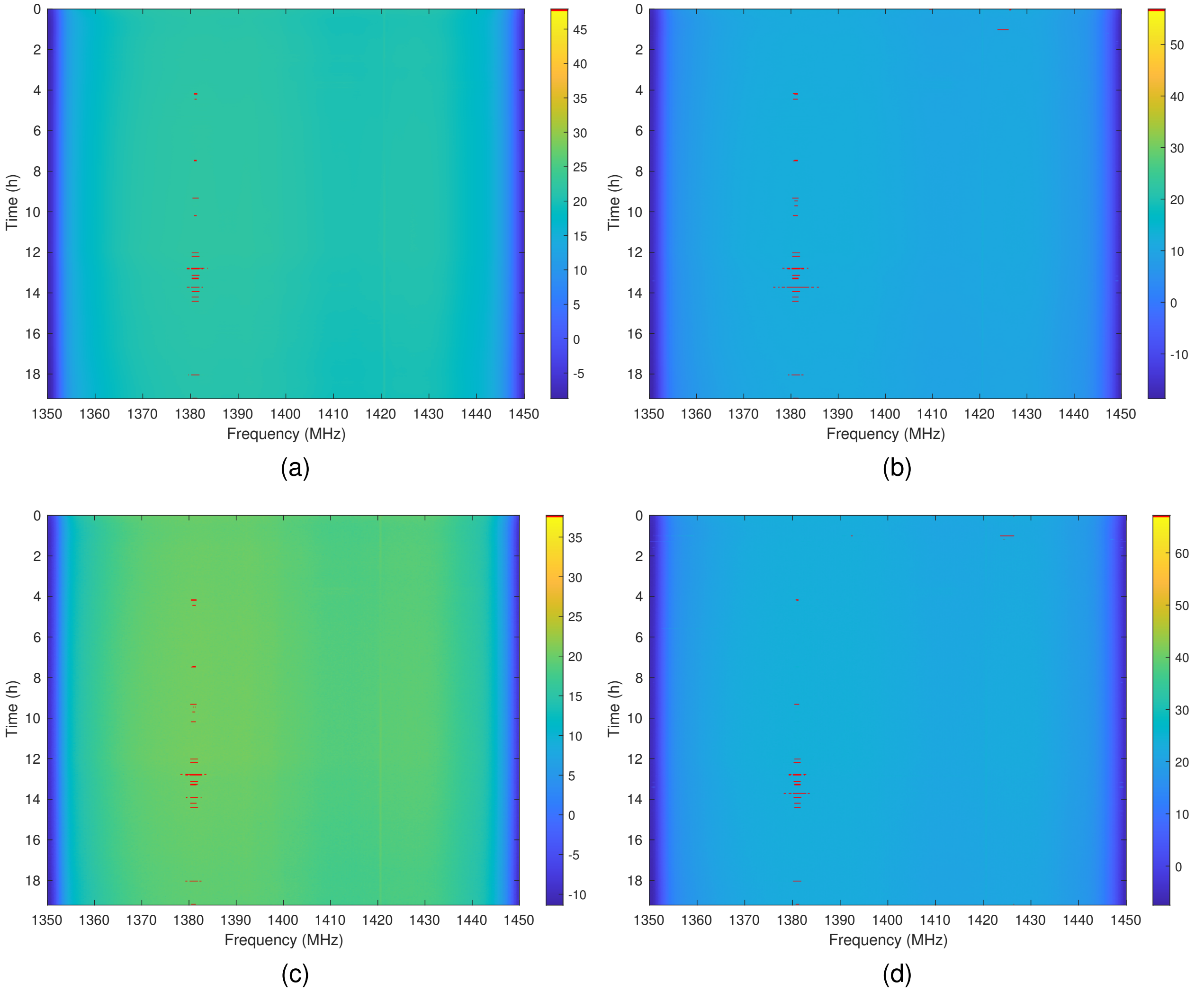

Fig. 9. Waterfall plots depicting four statistics used to detect RFI in the data. Red points represent values that exceed the masking threshold. The statistics are computed separately for each of the 500 frequency channels in the data, over a time period equal to one pulse period. The units are decibels with an arbitrary scale. The roll-off of the SDR front-end is visible at the band-edges. (a) Mean value, threshold $= 23\,\mathrm{dB}$. (b) Standard deviation, threshold $= 13\,\mathrm{dB}$. (c) Minimum value, threshold $= 21\,\mathrm{dB}$. (d) Maximum value, threshold $= 25\,\mathrm{dB}$.

that the estimation process will always provide estimates for $\hat{\phi}_{\text{off}}$ and $\hat{\text{SNR}}$, even if there is no actual pulsar signal present in the data. Therefore, some additional tests must be applied to verify that the measurement is valid.

The first test involves varying the DM value used to dedisperse the data. The dedispersion process presupposes B0329+54's known DM value of $26.76\,\mathrm{cm}^{-3}{\cdot}\mathrm{pc}$. It is expected that this DM value should result in the lowest minimum peak for the sum term in (7) compared to other, incorrect DM values. This can be verified by making no presuppositions about the DM value and varying it over a range to find the value that minimizes this sum term. An independent phase measurement is performed at each of the DM values that are searched. Fig. 13 shows the results of this search, which finds that the sum term is minimized at $30.8\,\mathrm{cm}^{-3}\cdot\mathrm{pc}$, which is near the expected DM value of $26.76\,\mathrm{cm}^{-3}\cdot\mathrm{pc}$. The minimum value, -1.909×10^5, lies on a flat part of the minimization curve and differs by only 0.16% from the value of -1.906×10^5 that occurs at the expected DM value.

A second test is an adaptation of a method previously used to determine the probability of false acquisition for GNSS signals [34]. It involves splitting the data into a number N of independent time segments and performing repeated pulse phase measurements. Since the total unmasked portion of the data amounted to just over $9\,\mathrm{h}$, the data can be split into $N = 9$ segments of length $1\,\mathrm{h}$ each. For each data segment, a phase offset measurement is performed. The method given by [34] is then used to bound the probability of false detection. First, a histogram is used to assign each measurement to one of L individual bins, and the most repeated value is determined. Since the width of the idealized top-hat pulse is approximately $1/50$ of the period, $L = 100$ was chosen as a conservative value. If an individual measurement agrees with the most repeated value within ±1 histogram bin, the measurement is called a "normal operation." The results of the 9 individual measurements are listed in Table V. The error column in Table V is computed relative to the mean value of the normal operations, which is equal to 0.3840. It

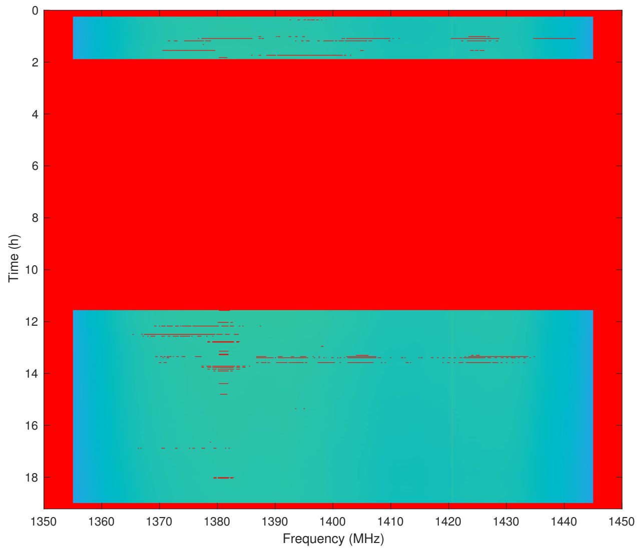

Fig. 10. Complete data mask used for the analysis. The first and last 15 minutes are masked, along with 9.67 h in the middle when the pulsar was below the elevation mask. Approximately 5 MHz at the upper and lower band edges is masked due to a roll-off in the frequency response of the SDR front-end. The remaining scattered points were masked due to exceeding one of the thresholds in Fig. 9. In total, 58.04% of the data points were masked.

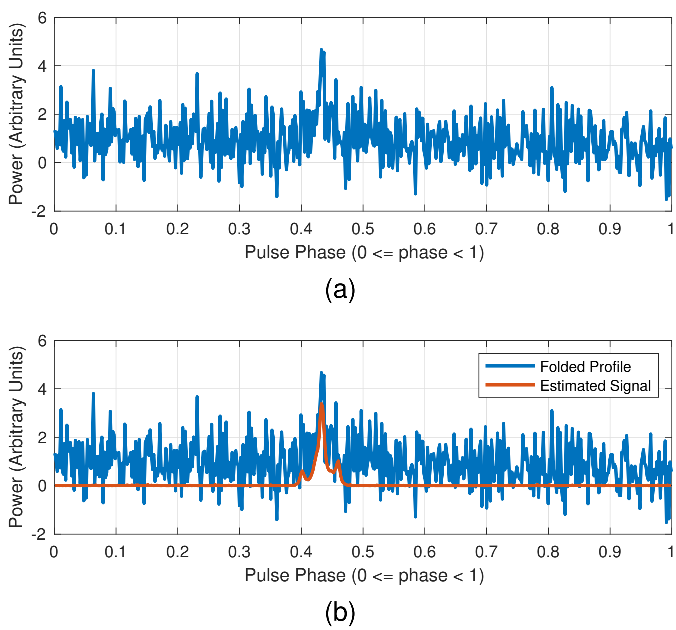

Fig. 11. (a) Dispersion-corrected integrated pulse profile $p[n]$ for the data set. (b) $p[n]$ is overlaid with $\hat{b}\tilde{s}[n]$, which is the template pulse profile after phase-shifting by $\hat{\phi}_{\text{off}}$ and scaling by $\hat{b}$. The estimated SNR is $5.90\,\text{dB}$.

should be noted that when the phase measurement does not succeed (a non-normal operation), the method used to estimate SNR does not apply such that the value computed for $\widehat{\text{SNR}}$ is meaningless. The total number of normal operations resulting from the N trials is denoted as K. It is assumed that if the pulsar signal is not present in the data, or if the SNR is not high enough to successfully perform a phase measurement, the phase measurement will be uniformly distributed over the L histogram bins. Since there are 3 possible bins for a valid measurement to land in, the single-trial probability of false

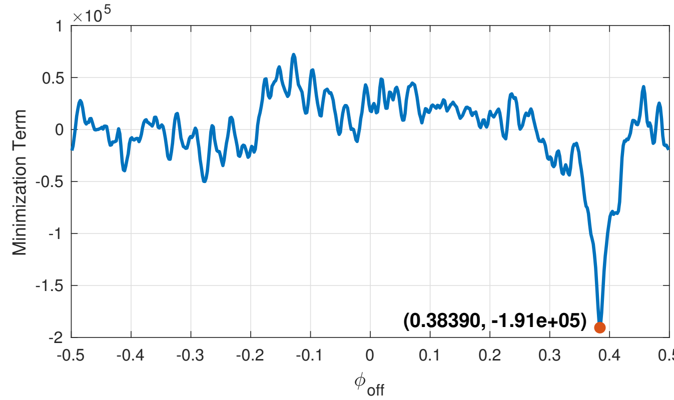

Fig. 12. Plot of the sum term in (7) vs. ϕ_{off}. The value of ϕ_{off} which minimizes the equation is found using Brent's method [29] and forms the phase offset estimate $\hat{\phi}_{\text{off}}$. This graph is conceptually similar to a cross-correlation peak.

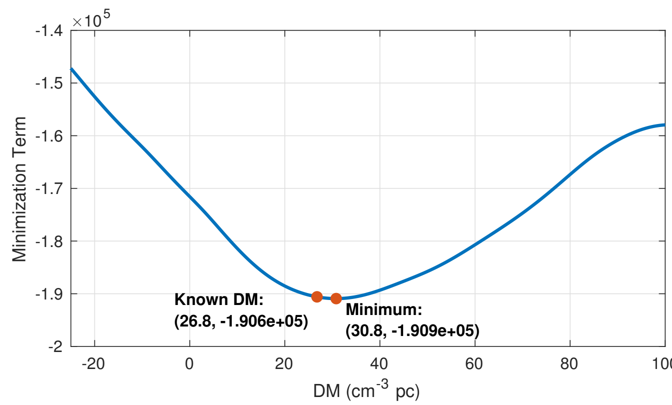

Fig. 13. Minimization of the sum term in (7) for a range of DM values. The value that results in the lowest minimum is close to the expected value of $26.76\,\text{cm}^{-3}\cdot\text{pc}$.

detection P_{fd} can be over-bounded [34]:

$$P_{\text{fd}} < 1/(L-3) \tag{16}$$

A threshold M is chosen such that a successful detection is declared when $K \geq M$. M should be chosen to be high enough such that the overall probability of false detection, denoted P_{FD}, is low. P_{FD} can be computed given the single-trial false detection probability [34]:

$$P_{\text{FD}} = L \sum_{i=M}^{N} \binom{N}{i} (1 - P_{\text{fd}})^{N-i} (P_{\text{fd}})^{i} \tag{17}$$

If M is chosen to be 4, then the overall false detection probability is 1.4×10^{-4}. For the measurements in Table V, 7 out of the 9 measurements are normal operations, such that $K = 7 > M$, and a successful detection is declared.

The third and final test involves plotting the estimated SNR and phase as a function of the total integration time t_{int}. According to (15), the SNR should increase proportionally to $\sqrt{t_{\text{int}}}$. Estimates of $\widehat{\text{SNR}}$ and $\hat{\phi}_{\text{off}}$ as a function of integration time were formed by truncating the data to various values of t_{int}. The results are displayed in Figs. 14 and 15. Fitting a function of the form $\text{SNR} = k\sqrt{t_{\text{int}}}$ to the data in Fig. 14 displays the expected relationship. Fig. 15 shows that the

TABLE V
INDIVIDUAL 1 h MEASUREMENTS.

Number	$\hat{\phi}_{\text{off}}$	Error	$\hat{\text{SNR}}$ (dB)	Normal Op
1	0.3826	-0.0014	1.84	Yes
2	0.3831	-0.0009	1.87	Yes
3	0.3820	-0.0020	2.12	Yes
4	**0.5685**	**+0.1845**	**2.22**	**No**
5	0.3864	+0.0024	3.44	Yes
6	**0.8006**	**+0.4166**	**0.56**	**No**
7	0.3870	+0.0030	3.29	Yes
8	0.3832	-0.0009	1.26	Yes
9	0.3838	-0.0002	1.87	Yes

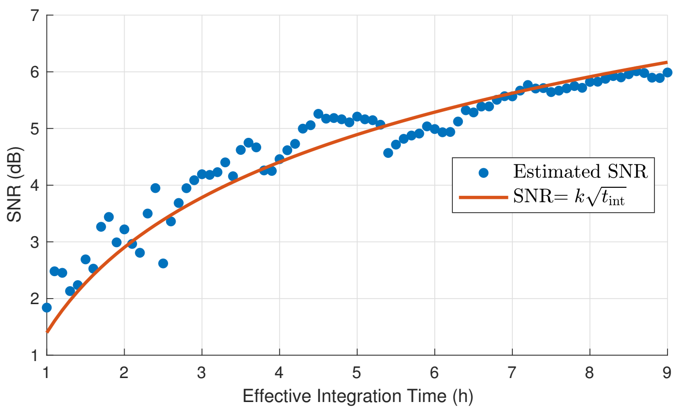

Fig. 14. Estimated SNR as a function of the total effective integration time t_{int}, overlaid with a curve fit to SNR $= k\sqrt{t_{\text{int}}}$. $k = 1.38$ when t_{int} is measured in hours.

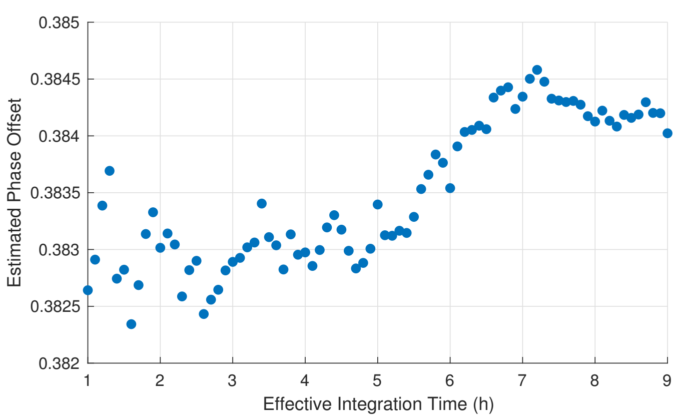

Fig. 15. Estimated phase offset $\hat{\phi}_{\text{off}}$ vs. effective integration time t_{int}.

variance of the phase offset estimate improves as a function of the integration time. The behavior exhibited between 5 and 7 h, where the value of the offset shifts upward slightly before converging on a different value, may be caused by the properties of the pulse shape. It is similar to the behavior exhibited by simulations of the pulsar conducted in [16].

The important parameters of the data collection are summarized in Table VI. The $5.90\,\text{dB}$ estimated SNR of the full data set is $3.25\,\text{dB}$ lower than the SNR of $9.15\,\text{dB}$ that was predicted by (15). This difference can most likely be attributed to unmodeled sources of noise in the system, unmitigated effects of RFI, inefficiencies in data processing, and the fact that the real pulsar profile is not an ideal top-hat shape as

TABLE VI
ANALYSIS PARAMETERS AND RESULTS FOR THE DATA COLLECTION.

Start Time (EDT)	8 June 2024 5:10 PM
End Time (EDT)	9 June 2024 12:23 PM
Total Length	19.22 h
File Size	553 GB
Effective Length (After Masking)	8.98 h
Effective Bandwidth (After Masking)	89.8 MHz
Number of Bins used for Folding	512
Estimated Post-Folding SNR	5.90 dB
Estimated Phase Offset	0.38390

assumed by (15). These cumulative effects serve to raise the effective noise level of the system. The effective total system noise temperature T_{sys} can be estimated by using the estimated SNR value of $5.90\,\text{dB}$ in (15) and solving for T_{sys}. This yields an estimated T_{sys} value of $100.1\,\text{K}$.

The standard deviation of the 7 normal operation phase measurements in Table V is equal to 1.9×10^{-3}. This standard deviation can be expressed in terms of time by multiplying it by the mean length of a pulse period during the data collection, $0.7145\,\text{s}$, yielding a timing standard deviation for these 7 measurements of $1.37\,\text{ms}$. The theoretical timing standard deviation can be computed based on the SNR using the following equation [35]:

$$\sigma_{\text{SNR}} = \frac{W_{\text{eff}}}{\text{SNR}\sqrt{n_{\text{bins}}}} \tag{18}$$

where W_{eff} is an effective pulse width computed from the samples of the template pulse:

$$W_{\text{eff}} = \frac{(P/W)\,T_0}{\left[n_{\text{bins}} \sum_{i=1}^{n_{\text{bins}}-1} \left(s[i] - s[i-1]\right)^2\right]^{1/2}} \tag{19}$$

W_{eff} is computed to be $55.1\,\text{ms}$. Using (15) and the values in Table IV but with t_{int} set to $1\,\text{h}$, the theoretical SNR for the $1\,\text{h}$ measurements is computed to be $3.89\,\text{dB}$ and $\sigma_{\text{SNR}} = 0.99\,\text{ms}$.

VII. CONCLUSIONS

The experiment was successful in observing pulsar B0329+54 and measuring its pulse phase using an antenna with an effective aperture of $1.45\,\text{m}^2$. The estimated SNR after an integration period of $8.98\,\text{h}$ was $5.90\,\text{dB}$, suggesting that the effective system noise temperature T_{sys} was approximately $100.1\,\text{K}$. In addition, 7 independent phase measurements with an integration time of $1\,\text{h}$ each were successfully performed. The standard deviation of these 7 phase measurements, expressed in units of time, was $1.37\,\text{ms}$, which is only $0.38\,\text{ms}$ higher than the theoretical standard deviation of $0.99\,\text{ms}$. The results of the experiment demonstrate the feasibility of using a small aperture antenna to perform phase measurements of pulsar signals. The observed SNR was $3.25\,\text{dB}$ lower than the expected SNR, which can be attributed to unmodeled sources of noise in the system, unmitigated RFI effects, inefficiencies in data processing, and the idealized assumptions of the expected SNR computation.

For future studies, a larger data set could be collected over a period of multiple days, allowing for several independent phase measurements with integration times greater than $1\,\mathrm{h}$ to be performed. It is expected that phase measurement accuracy, like SNR, scales as a factor of $\sqrt{t_{\text{int}}}$ [2]. A larger data set will enable a thorough investigation of this relationship. Additionally, multiple data sets could be recorded over a time span of weeks or months, allowing for the evaluation of long-term relative stability of the phase measurements. It is expected that a performance improvement could be achieved by taking advantage of the dual-polarization feed to record two orthogonal polarizations simultaneously. According to (15), the use of two polarizations could increase the SNR by a factor of $\sqrt{2}$. Further tuning and optimization of the dedispersion process or alternative dedispersion methods could also result in SNR improvements [25]. While this experiment was conducted at a remote location to obtain a relatively clean RF environment, future experiments could be conducted in more challenging environments which may necessitate the use of improved RFI mitigation techniques.

Acknowledgments

The authors would like to thank Zachary Arnett, Alex Burnett, and Paul Nilles of Ohio University for their assistance in setting up the experiment hardware and Mark Collier of Ryco Electric for allowing the use of his land and facilities for the experiment. The authors would also like to thank the reviewers for their constructive comments and suggestions.

References

[1] A. Hewish, S. J. Bell, J. D. H. Pilkington, P. F. Scott, and R. A. Collins, "Observation of a rapidly pulsating radio source," *Nature*, vol. 217, pp. 709–713, Feb. 1968, doi: 10.1038/217709a0.

[2] D. Lorimer and M. Kramer, *Handbook of Pulsar Astronomy*. Cambridge, U.K.: Cambridge Univ. Press, 2005.

[3] Australia Telescope National Facility. The ATNF pulsar catalogue. [Online]. Available: https://www.atnf.csiro.au/research/pulsar/psrcat/

[4] G. Hobbs *et al.*, "A pulsar-based time-scale from the international pulsar timing array," *Monthly Notices Roy. Astronomical Soc.*, vol. 491, no. 4, pp. 5951–5965, Feb. 2020, doi: 10.1093/mnras/stz3071.

[5] G. Agazie *et al.*, "The NANOGrav 15 yr data set: Evidence for a gravitational-wave background," *Astroph. J. Lett.*, vol. 951, no. 1, p. L8, Jun. 2023, doi: 10.3847/2041-8213/acdac6.

[6] J. W. Mitchell *et al.*, "Station explorer for X-ray timing and navigation technology architecture overview," in *Proc. 27th Int. Tech. Meeting Sattel. Division Inst. Navig. (ION GNSS+ 2014)*, Tampa, FL, USA, Sep. 2014, pp. 3194–3200.

[7] L. M. B. Winternitz *et al.*, "X-ray pulsar navigation algorithms and testbed for SEXTANT," in *2015 IEEE Aerosp. Conf.*, Big Sky, MT, USA, Mar. 2015, doi: 10.1109/AERO.2015.7118936.

[8] W. Zhang *et al.*, "X-ray pulsar navigation based on phase and doppler frequency shift using double-differenced," *IEEE Trans. Instrum. Meas.*, vol. 73, Apr. 2024, doi: 10.1109/TIM.2024.3393539.

[9] J. W. Mitchell *et al.*, "SEXTANT X-Ray pulsar navigation demonstration: Initial on-orbit results," in *Proc. 41st Annu. AAS Guid. and Control Conf. (AAS/GNC 2018)*, Breckenridge, CO, USA, Feb. 2018, AAS 18-155.

[10] L. B. Winternitz *et al.*, "A high-fidelity performance and sensitivity analysis of x-ray pulsar navigation in near-Earth and cislunar orbits," in *Proc. 44th Annu. AAS Guid. and Control Conf. (AAS/GNC 2022)*, Breckenridge, CO, USA, Feb. 2022, AAS 22-072.

[11] G. S. Downs, "Interplanetary navigation using pulsating radio sources," Jet Propulsion Laboratory, Pasadena, CA, USA, NASA Technical Reports N74-34150, Oct. 1974.

[12] G. Tavares, D. Brito, and J. Fernandes, "A study on the accuracy of radio pulsar navigation systems," in *Proc. Eur. Navig. Conf. 2015 (ENC 2015)*, Bordeaux, France, Apr. 2015.

[13] R. McKnight and F. van Graas, "Radio-frequency pulsar observation using small-aperture antennas," in *Proc. 2022 Int. Tech. Meeting Inst. Navig.*, Long Beach, CA, USA, Jan. 2022, pp. 856–866, doi: 10.33012/2022.18259.

[14] A. Jessner, "Technical requirements for autonomous space craft navigation using radio pulsars," in *Proc. 593rd WE-Heraeus Seminar on Autonomous Spacecraft Navig.*, Bad Honnef, Germany, Jun. 2015.

[15] R. McKnight, Z. Arnett, B. C. Peters, and S. Ugazio, "Performance characterization for a small-aperture radio-frequency pulsar experiment," in *Proc. 35th Int. Tech. Meeting Satell. Division Inst. Navig. (ION GNSS+ 2022)*, Denver, CO, USA, Sep. 2022, pp. 1933–1941, doi: 10.33012/2022.18543.

[16] R. McKnight, B. C. Peters, Z. Arnett, and S. Ugazio, "Analysis of small-aperture radio-frequency pulsar data," in *Proc. 2024 Int. Tech. Meeting Inst. Navig.*, Long Beach, CA, USA, Jan. 2024, pp. 770–777, doi: 10.33012/2024.19494.

[17] International Telecommunication Union Radiocommunication Sector, "Preferred frequency bands for radio astronomical measurements below 1 THz," Recommendation ITU-R RA.314-11, Dec. 2023. [Online]. Available: https://www.itu.int/rec/R-REC-RA.314-11-202312-I

[18] D. R. Lorimer, J. A. Yates, A. G. Lyne, and D. M. Gould, "Multifrequency flux density measurements of 280 pulsars," *Monthly Notices Roy. Astronomical Soc.*, vol. 273, pp. 411–421, Mar. 1995, doi: 10.1093/mnras/273.2.411.

[19] A. von Hoensbroech and K. M. Xilouris, "Effelsberg multifrequency pulsar polarimetry," *Astron. & Astrophys. Suppl. Ser.*, vol. 126, pp. 121–149, Nov. 1997, doi: 10.1051/aas:1997255.

[20] Jodrell Bank Pulsar Group. The EPN database of pulsar profiles. [Online]. Available: https://psrweb.jb.man.ac.uk/epndb/

[21] D. R. Lorimer *et al.*, "A flexible format for exchanging pulsar data," *Astron. & Astrophys. Suppl. Ser.*, vol. 128, no. 3, pp. 541–544, Mar. 1998, doi: 10.1051/aas:1998161.

[22] G. Hobbs, A. G. Lyne, M. Kramer, C. E. Martin, and C. Jordan, "Long-term timing observations of 374 pulsars," *Monthly Notices Roy. Astronomical Soc.*, vol. 353, no. 4, pp. 1311–1344, Oct. 2004, doi: 10.1111/j.1365-2966.2004.08157.x.

[23] T. E. Hassall *et al.*, "Wide-band simultaneous observations of pulsars: disentangling dispersion measure and profile variations," *Astron. & Astrophys.*, vol. 543, p. A66, Jul. 2012, doi: 10.1051/0004-6361/201218970.

[24] G. B. Hobbs, R. T. Edwards, and R. N. Manchester, "TEMPO2, a new pulsar-timing package – I. an overview," *Monthly Notices Roy. Astronomical Soc.*, vol. 369, no. 2, pp. 655–672, Jun. 2006, doi: 10.1111/j.1365-2966.2006.10302.x.

[25] W. van Straten and M. Bailes, "DSPSR: Digital signal processing software for pulsar astronomy," *Publications Astronomical Soc. Aust.*, vol. 28, pp. 1–14, 2011, doi: 10.1071/AS10021.

[26] R. N. Bracewell, *The Fourier Transform and its Applications*, 3rd ed. New York, NY, USA: McGraw Hill, 2000.

[27] J. H. Taylor, "Pulsar timing and relativistic gravity," *Philos. Trans. Roy. Soc. London. Ser. A: Physical and Eng. Sci.*, vol. 341, no. 1660, pp. 117–134, Oct. 1992, doi: 10.1098/rsta.1992.0088.

[28] J. Wang *et al.*, "A comparative analysis of pulse time-of-arrival creation methods," *Astron. & Astrophys.*, vol. 658, p. A181, Feb. 2022, doi: 10.1051/0004-6361/202141121.

[29] W. H. Press, S. A. Teukolsky, W. T. Vetterling, and B. P. Flannery, *Numerical Recipes: The Art of Scientific Computing*, 3rd ed. Cambridge, U.K.: Cambridge University Press, 2007.

[30] D. Bhattacharya, "Detection of radio emission from pulsars," in *The Many Faces of Neutron Stars (NATO ASI Ser.)*, R. Buchheri, J. van Paradijs, and A. Alpar, Eds., 1998, pp. 103–128.

[31] F. van Graas, C. Cohenour, N. Norris, E. Vinande, S. Gunawardena, and M. Carroll, "GNSS signal characterization and monitoring using high gain antennas," in *Proc. 28th Int. Tech. Meeting Satell. Division Inst. Navig. (ION GNSS+ 2015)*, Sep. 2015, pp. 3426–3433.

[32] A. De Oliveira-Costa, M. Tegmark, B. M. Gaensler, J. Jonas, T. L. Landecker, and P. Reich, "A model of diffuse galactic radio emission from 10 MHz to 100 GHz," *Monthly Notices Roy. Astronomical Soc.*, vol. 388, no. 1, pp. 247–260, Jul. 2008, doi: 10.1111/j.1365-2966.2008.13376.x.

[33] J. D. Kraus, *Radio Astronomy*, 2nd ed. Durham, NH, USA: Cygnus-Quasar Books, 1986.

[34] Z. Zhu, F. van Graas, and J. Starzyk, "GPS signal acquisition using the repeatability of successive code phase measurements," *GPS Solutions*, pp. 43–53, Jan. 2008, doi: 10.1007/s10291-007-0064-x.

[35] M. T. Lam *et al.*, "The NANOGrav nine-year data set: Noise budget for pulsar arrival times on intraday timescales," *Astroph. J.*, vol. 819, no. 2, p. 155, Mar. 2016, doi: 10.3847/0004-637X/819/2/155.

VIII. Biography Section

Ryan McKnight (Graduate Student Member, IEEE) received the B.S. and M.S. degrees in electrical engineering from Ohio University, Athens, OH, USA in 2019 and 2023, respectively. He is currently pursuing the Ph.D. degree in electrical engineering and computer science at Ohio University.

Since 2019, he has been a Graduate Research Assistant for the Ohio University Avionics Engineering Center, where he works on positioning, navigation, and timing research. Since 2022, he has worked as a Pathways Intern at NASA Goddard Space Flight Center, Greenbelt, MD, USA, where he is involved with the development of the NavCube3-mini lunar global navigation satellite systems receiver.

Mr. McKnight is a member of the Institute of Navigation (ION). In 2023, he was the recipient of the IEEE Aerospace and Electronic Systems Society Graduate Engineering Scholarship.

Brian C. Peters (Graduate Student Member, IEEE) received the B.S. and M.S. degrees in electrical engineering from Ohio University, Athens, OH, USA, in 2019 and 2021, respectively. He is currently pursuing the Ph.D. degree in electrical engineering and computer science at Ohio University.

From 2019-2021, he was a Graduate Research Assistant at the Avionics Engineering Center, Ohio University, where he was involved in research in the enhancement of global navigation satellite systems interoperability. From 2021-2022, he was a Navigation Systems Engineer at Advanced Space, Westminster, CO, USA. He is currently a Pathways Intern at NASA Goddard Space Flight Center, Greenbelt, MD, USA, where he supports the Lunar Communications Relay and Navigation Systems (LCRNS) project.

Sabrina Ugazio (Member, IEEE) received her B.S. and M.S. degrees in Electrical Engineering from Politecnico di Torino, Italy, in 2007 and 2009, respectively, and earned her Ph.D. in Electrical Engineering and Telecommunications from the same institution in 2013.

At Politecnico di Torino, she joined the Navigation Signal Analysis and Simulation (NavSAS) research group in 2009 as an M.S. student and continued her work there as a postdoctoral researcher from 2013 to 2016. She is currently an Assistant Professor at the Ohio University School of Electrical Engineering and Computer Science (EECS), which she first joined as a Visiting Ph.D. student in 2011-2012 and later as a Visiting Assistant Professor in 2016 to 2019. At Ohio University, she is also a faculty member of the Avionics Engineering Center (AEC).

Dr. Ugazio's research focuses on global navigation satellite systems (GNSS) and integrated navigation systems, with an emphasis on avionics and space applications. She is a member of The Institute of Navigation (ION).

Frank van Graas (Senior Member, IEEE) received the B.S. and M.S. degrees in electrical engineering from Delft University of Technology, Delft, The Netherlands in 1983 and 1985, respectively, and the Ph.D. degree in electrical engineering from Ohio University, Athens, OH, USA, in 1988.

From 1988 to 2021, he was an electrical engineering faculty member at Ohio University, Athens, OH, USA. His research involved global navigation satellite systems, signal processing and integrated navigation systems. He is currently a Research Professor of electrical engineering at the Air Force Institute of Technology, WPAFB, OH, USA.

Dr. van Graas is a member of The Institute of Navigation (ION) and the American Institute of Aeronautics and Astronautics. He is a Past President and Fellow of The ION. In 1996 he received the Johannes Kepler Award for "sustained and significant contributions to satellite navigation," from the Satellite Division of The ION. In 2002, he received the Colonel Thomas L. Thurlow Award for "outstanding contribution to the science of navigation," from the ION. In 2011, he received the John Ruth Avionics Award from the AIAA for "Outstanding Lifetime Achievement in the Area of GPS Navigation."